

Feature Extraction Reimagined: Achieving Superior Accuracy in Camera Calibration

Zezhun Shi
Independent Researcher

Abstract

Camera calibration is crucial for 3D vision applications. This paper focuses on improving the accuracy of feature extraction, which is a key step in calibration. We address the aliasing problem of star-shaped pattern by introducing a novel dynamic calibration target that synthesizes multiple checkerboard patterns of different angle around pattern center, which significantly improves feature refinement accuracy. Additionally, we propose a novel cost function of feature refinement that accounts for defocus effect, offering a more physically realistic model compared to existing symmetry based method, experiment on a large dataset demonstrate significant improvements in calibration accuracy with reduced computation time. Our code is available from <https://github.com/spdfghi/Feature-Extraction-Reimagined-Achieving-Superior-Accuracy-in-Camera-Calibration.git>.

1. Introduction

Camera calibration is fundamental to 3D vision, with broad applications in autonomous driving, robotics, architecture, medicine, etc. Camera calibration primarily serves two purposes: first, to establish a mapping between three-dimensional homogeneous coordinates (rays originating from the camera) and pixel points, known as intrinsic calibration; and second, to calibrate the positional relationship between the camera and other cameras [14, 33] or types of sensors, such as LiDAR [22], known as extrinsic calibration. Camera calibration methods are mainly divided into those based on target based calibration and online self-calibration methods [17], depending on the input. In certain scenarios, such as aerial robots, extrinsics can undergo significant changes even with moderate shocks or during extended operations in environments with vibrations, making self-calibration important. However, since intrinsic parameters remain relatively stable even in challenging conditions [33] and target based calibration accuracy advantage over self-calibration, they dominate in most scenarios and

are a necessary preliminary step for multi-sensor extrinsic calibration.

Camera intrinsic calibration is mainly divided into three steps: feature extraction, parameter initialization, and nonlinear optimization. Camera models can be classified into two categories: physics-based parametric models and purely mathematical generic models. In physical models, geometric calibration assumes that the camera generally follows the pinhole camera projection model, while also considering the nonlinear effect of the lens on the light rays, leading to what is known as distortion. The two main types of distortion models are the Brown-Conrady model [5, 7] and the Thin-Prism Fisheye model [31]. Generally, during model initialization, distortion is ignored, and an initial estimate of the camera matrix is obtained. Zhang et al. [32] proposed a initialization method based on the algebraic relationships of homography matrices between control points in multiple 2D planes, which is flexible and commonly used. After initialization, the nonlinear optimization step is used to calculate distortion parameters and refine the camera matrix elements. The widely adopted approach is to use sum of reprojection error norm as the cost function, there are also other kind of cost functions such as the one base on line straightness metric [4]. The generic camera model only considers the correspondence between pixel points and 3D observation lines[9, 16, 23, 25], Ref. [9] also consider parameter of defocus. The initialization of generic model is thoroughly considered in Ref. [23], Schöps et al. [25] extended their method, achieving more accurate feature extraction and provided full bundle adjustment (BA) optimization.

Parameter initialization and nonlinear optimization are purely mathematical problems that have been extensively explored, while feature extraction is still an open task. As the first step of calibration, feature extraction and refinement ultimately determines the accuracy in most cases and is the focus of this paper. The two main calibration pattern are the circle and checkerboard. The former generally provides higher accuracy but is limited by distortion, whereas the latter does not have this problem [3, 12, 13]. The main issue with the circle pattern is that the shape of circle un-



Figure 1. **Left:** Checkerboard. **Middle:** Deltille [11]. **Right:** Star-shaped pattern [25]. These three calibration patterns feature an increasing number of intersecting lines, resulting in progressively higher image gradient information. However, as the number of intersecting lines increases, aliasing at the center becomes more pronounced.

der distortion can hardly be calculated. Recently, Song et al. [26] proposed an impressive analytical method to solve this problem, which computes the centroid rather than fitting the shape of a distorted circle. But this method still has limitations. For accurate centroid calculation, the circle must be sufficiently large, which restricts the ability to estimate for distortion near the image boundaries.

To improve the detection accuracy of checkerboard pattern, a series of methods have been studied. Currently, two mainstream approaches are notable. The first is assuming vector from a corner to its adjacent area pixel is orthogonal to pixel’s gradient direction [8], such as implemented in OpenCV, which achieve good sub-pixel accuracy; however, its performance is subpar under some conditions, as tested by Song et al. [26] with infrared cameras. Datta et al. discovered that the assumption of OpenCV does not hold in non fronto-parallel input images [3]. Therefore they iteratively estimate the homography matrix and distortion, then extract point after a transform to canonical fronto-parallel image, which result in a significantly improvement. The second approach involves quadratic surface fitting [18], commonly used in MATLAB. Fitting methods not only apply to regular checkerboards but have also been extended to curved surface[29]. Ha et al. [11] expanded the fitting method to Deltille pattern which has three intersecting lines(Fig. 1), where they got better reprojection error than checkerboard. Schöps et al. [25] further developed Ha’s pattern by using a star-shaped calibration board with eight intersecting lines, they also proposed a novel feature refinement algorithm [24, 25], which takes cost by pixel differences in projections of symmetric world points. With more gradient information, they got significant improvement in accuracy.

However, their experiments show that best segment number range of star-shaped pattern is 12 to 20. Exceeding this number actually leads to an increase in reprojection error. They attribute this to the fact that monitor and camera cannot resolve more intersecting line patterns, i.e., the problem of aliasing caused by defocus and pixel discretization. To

solve this problem, we employed a novel calibration pattern that consists of a video synthesized from a series of checkerboard patterns rotating around center of the pattern. By capturing these patterns at different time and then combining the captured images into a multi-channel image, we can separate areas that would otherwise experience aliasing into distinct layers, thereby solved this problem. Our experiments demonstrated the accuracy advantage against the optimal star-shaped pattern under same segmentation, with further improvements in accuracy as the segmentation increases.

In addition, we carefully considered their cost function for feature refinement. First, it implicitly assumes that the image is captured by a pinhole camera of a continuous physical pattern, and that there should not be significant distortion. Then, they assume that the image vary smoothly among neighbor pixels. Regarding the former, we believe that the assumption of a continuous physical pattern does not always hold. Although infrared radiation is generated by molecular thermal motion, which may lead to blurred physical patterns in infrared-based cameras, this is not the case for commonly used visible light cameras, which captures light reflected by objects and is related to the object’s color. Abrupt changes can occur within the range of a single pixel [27], and defocus is the dominant factor for blur. Thus, we proposed a more physical cost function by considering of defocus. We conducted experiments on the calibration of a generic camera model using a dataset of over one thousand images, achieving significantly lower reprojection errors. Moreover, our cost function is simpler with fewer parameters, which means reduced computation time and a lower risk of overfitting. We also do a math on their smooth assumption by study a blur line model, which is the convolution of 2D step function with a Gaussian kernel. We provided explicit expression for pixel value and used it to study the variation of differences against intensity of pixel center.

As a summary, there are two main contributions of this paper:

- We propose a novel camera calibration system that addresses the aliasing issue in patterns based on multiple intersecting lines. This system provides superior calibration accuracy, while its shape remains unaffected by distortion, similar to the basic checkerboard pattern.
- We propose a symmetry based cost function for feature refinement of checkerboard-like corner. This method shows significant accuracy and speed improvements compared with existing symmetry based approach.

2. Related Works

Camera Calibration under defocus Duda et al. [6] proposed a method based on localized Radon transform approximated by box filters, compared to the OpenCV

method, it is more robust to noise and blur, achieving significant accuracy improvements in outdoor environments. Ha et al. [10] introduced an active targets approach for calibration under defocus, they separated the checkerboard into overlapping horizontal and vertical stripes, and then applied a novel deconvolution method to these stripes. Further, they do a refraction correction of the glass screen. This method was evaluated on real data, and shows accurate camera calibration result under severe defocus.

Their pattern shares some design similarities with ours, as both approaches decompose existing patterns into multiple simpler ones and then perform calibration dynamically. However, there are three notable differences: Firstly, their pattern is designed primarily to simplify deconvolution operations rather than address aliasing; they use only a decomposition of a checkerboard pattern, whereas our pattern, similar to star-shaped calibration board, provides more gradients. Secondly, they model defocus with a Gaussian function followed by deconvolution for feature refinement, while we leverage symmetry to implicitly account for defocus, making it more adaptable to various camera types. Lastly, our pattern does not rely on a display screen, by changing the pattern shape from square to circular, it can be manufactured mechanically, which is more flexible.

Active target has also been applied in various patterns, some researchers used phase information which they considered more robust in defocusing scenes than checkerboard [15, 20], and phase-shift method for camera calibration has been developed in recent years. These methods mainly contain sets up sinusoidal stripes [30] or circular patterns [2] sequentially displayed on an LCD monitor and detect sub-pixel feature points from phase map, which is calculated by phase-shifting algorithm. And with neural network for feature extraction, progress has been made in difficult tasks such as large field-of-view stereo calibration [20].

Line Detection under Defocus. The classic Canny algorithm obtains single-pixel edges through non-maximum suppression, and Devernay et al. further refines edges to sub-pixel accuracy using quadratic fitting near maxima [28]. While these well-known methods assume edge is maxima of smooth function, Ref. [27] first considers the physical scenario of a straight edge partially falling within a pixel. By analytically integrating the area segmented by the line within one pixel, it shows the discontinuity of discrete pixels will generate bias with traditional gradient computation. But they didn't provide an analytical result considering defocus. The calibration pattern used by Ha et al. [10] can actually be considered as lines under defocus, where they proposed an deconvolution method but also without using analytical formula. The analytical expression for line defocus was first introduced in Ref. [21] and used in Ref. [34] for single-image defocus estimation. Bakery et al. [1] con-

sidered the pixel value rather than point value expression, which was not addressed in Ref. [21]. The line defocus model used in this paper is similar to Bakery et al., the difference is that their paper focused on using numerical methods to construct a feature detector. They only provided an integral form while we provide explicit results.

3. Method

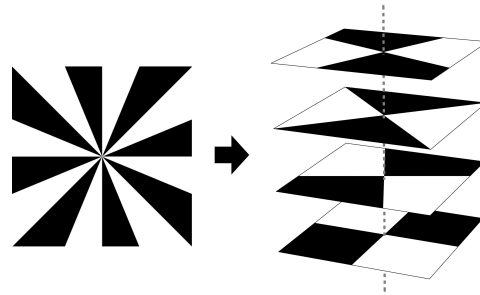


Figure 2. **Left:** Star-shaped pattern, which shows better result for camera calibration than checkerboard and Deltille grid [25]. **Right:** Proposed method. To solve the aliasing problem, we decompose the star-shaped pattern into a series of checkerboard patterns, then extract them from the captured video stream and stack them into a multi-channel image.

3.1. Pattern design

Clearly, the aliasing of the star-shaped pattern in the captured images is caused by a combination of physical material properties, defocus, and pixel discretization. The first two factors are inevitable and occur in all kinds of patterns. Our design primarily addresses the latter, where multiple intersecting lines within a pixel range dominate. The key idea is that, unlike the star pattern board, which captures all intersecting line patterns in a single image, we instead extract gradient information from a series of checkerboard patterns rotated around the center of the pattern, see Fig. 2. These rotated-checkerboard images are then combined into a multi-channel image, i.e., we separate the information of spatially aliased pixels into different channels.

To obtain the checkerboard patterns rotated around the local centers, we cyclically display the calibration images from Fig. 3 on the screen. Then, from the video stream captured by the camera, we obtain stable frames based on the pixel differences between adjacent frames, and use the AprilTag to distinguish the rotation angles of different checkerboard patterns. These stable frames are combined into a multi-channel image, which is then used for feature optimization with the cost function from Sec. 3.3. We combine these images into a multi-channel format for

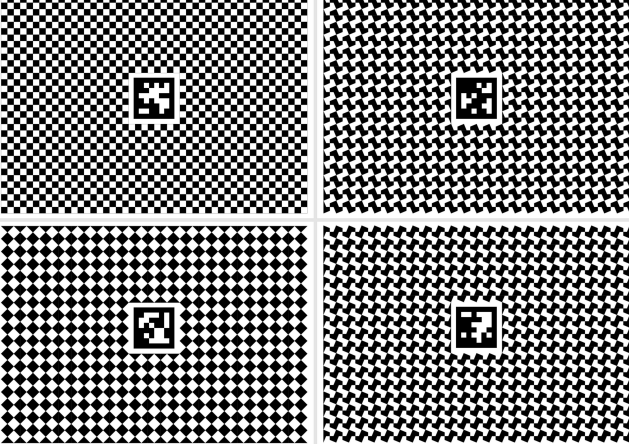


Figure 3. **Example of our calibration pattern.** The top-left image is identical to the 4 segments star pattern in Schöps et al.’s work, while the other three images rotate each pattern element by $\pi/8$ around its local center. These images are displayed sequentially on the screen. For the central AprilTag, Schöps et al. used it for pattern localization and feature initialization, whereas we also utilize its index to determine the corresponding channel of the composite image.

two reasons: first, it integrates multiple calibration patterns, thereby mitigating system bias introduced by random sampling in our algorithm; second, it is cache-efficient, enhancing computational performance.

3.2. A Gaussian defocus model

Before introducing our cost function for feature refinement, we would like to discuss pixel continuity and the effect of image blur on interpolation. In the absence of blur, traditional subpixel techniques tend to produce significant deviations near image boundaries, which is the so called partial area effect[27]. A simple example involves two horizontally adjacent pixels, j and $j + 1$, with a vertical boundary dividing pixel j into two equal area, where the intensities of the two parts are W and B , respectively, while the intensity of all positions in pixel $j + 1$ is B . See Fig. 4. Using linear interpolation yields an intensity of $(W + 3B)/4$ at the location between the two pixels, which differs significantly from the true intensity B . Intuitively, Gaussian blur can reduce this discrepancy, and we will provide a quantitative discussion of this effect in this section. It is worth noting that this issue also arises in the feature refinement problem where Datta et al. shows that OpenCV’s method doesn’t work well [3].

Checkerboard feature points can be viewed as corner points where two lines intersect, we model the original image of line that captured by a noise-free pinhole camera as step function [1]

$$\mathcal{I}_o(\mathbf{p}|d) = \begin{cases} W, & d \geq 0 \\ B, & d < 0 \end{cases} \quad (1)$$

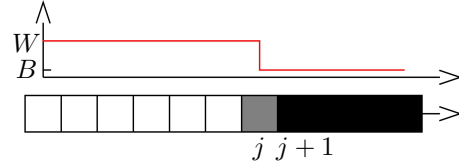


Figure 4. **Interpolation problem.** The image above shows the actual light intensity of a one-dimensional edge image, while the image below represents the result of pixel discretization.

where W and B denote constant intensity of white and black region, and d represents the distance from point \mathbf{p} to the line passing through the feature center \mathbf{q} . Let θ denotes the angle from image x-axis to the line, one can compute d through a simple dot product

$$d(\mathbf{p}|\mathbf{q}, \theta) = \mathbf{n}_x(\theta) \cdot (\mathbf{q} - \mathbf{p}). \quad (2)$$

Where we build coordinate that y axis is along direction of the line and \mathbf{n}_x is the normal vector of x axis. Note that the two half-planes divided by the line are not identical, so d is a signed quantity.

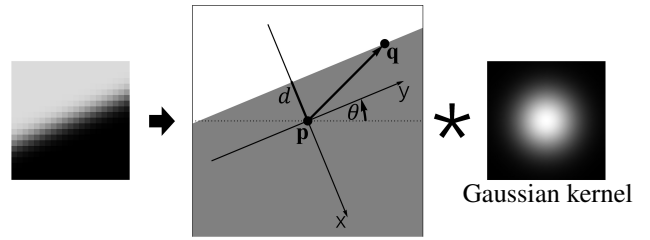


Figure 5. **Line defocus model.** Left simulation is generated using Eq. (8) with $W = 250$, $B = 50$, $\theta = \pi/8$, $\sigma = 1.5$ and $\mathbf{q} = (0, 0)$.

For optical camera, we need to consider the defocus factor and optical transfer function. Bakery et al. [1] modeled these effects as a Gaussian kernel function, which is a widely used [10, 21, 34] approach. 2-D Gaussian has the form

$$\mathcal{K}(x, y|\sigma) = \frac{1}{2\pi\sigma^2} e^{-\frac{x^2+y^2}{2\sigma^2}}. \quad (3)$$

The real blur image can be calculated as a convolution of noise-free pinhole image with the kernel. Due to the symmetry of Gaussian function, the convolution to a straightforward integration

$$\begin{aligned} & \mathcal{I}_{pt}(\mathbf{p}|d, \sigma) \\ &= \mathcal{I}_o(\mathbf{p}|d) * \mathcal{K}(x, y|\sigma) \\ &= \frac{1}{\sqrt{2\pi\sigma^2}} \left[W \int_{-\infty}^d e^{-\frac{x^2}{2\sigma^2}} dx + B \int_d^{\infty} e^{-\frac{x^2}{2\sigma^2}} dx \right], \quad (4) \\ &= \frac{W - B}{2} \operatorname{erf} \left(\frac{d}{\sqrt{2}\sigma} \right) + \frac{W + B}{2} \end{aligned}$$

where erf is the error function

$$\text{erf}(t) = \frac{2}{\sqrt{\pi}} \int_0^t e^{-x^2} dx, \quad (5)$$

implemented by most numerical program language, like C and Matlab. Using integration by parts, we can obtain the integral

$$\int_a^b \text{erf}(t) dt = \frac{e^{-t^2}}{\sqrt{\pi}} + t \text{erf}(t) \Big|_a^b, \quad (6)$$

and integrate again we get

$$\int_a^b \left[\frac{e^{-t^2}}{\sqrt{\pi}} + t \text{erf}(t) \right] dt = \frac{1}{4} (2t^2 + 1) \text{erf}(t) + \frac{e^{-t^2} t}{2\sqrt{\pi}} \Big|_a^b. \quad (7)$$

From above two equations, we then can obtain the i -th pixel value by performing integral over a rectangular region centered at (x_i, y_i) . For the sake of brevity, we have omitted parameters $\mathbf{q}, \theta, \sigma$ from main expression and leaved the dependence to its variable α and δ_k

$$\begin{aligned} & \mathcal{I}_{px}(i|\mathbf{q}, \theta, \sigma) \\ &= \int_{y_i - \frac{1}{2}}^{y_i + \frac{1}{2}} \int_{x_i - \frac{1}{2}}^{x_i + \frac{1}{2}} \mathcal{I}_{pt}(\mathbf{p}|d, \sigma) dp_x dp_y, \quad (8) \\ &= \alpha \sum_{k=1}^4 s_k \left[(2\delta_k^2 + 1) \text{erf}(\delta_k) + \frac{2}{\sqrt{\pi}} e^{-\delta_k^2} \delta_k \right] + \beta \end{aligned}$$

where

$$\alpha(\theta, \sigma) = \frac{(W - B)\sigma^2}{2 \sin(2\theta)}, \quad \beta = \frac{W + B}{2}, \quad (9)$$

and δ_k is the distance function Eq. 2 of four corner of pixel to the line, with a scaling factor

$$\delta_k(\theta, \mathbf{q}, x_i, y_i) = \frac{1}{\sqrt{2}\sigma} d((x_i + r_k, y_i + t_k)|\mathbf{q}, \theta). \quad (10)$$

k	s_k	r_k	t_k	k	s_k	r_k	t_k
1	1	-1/2	-1/2	3	1	+1/2	+1/2
2	-1	+1/2	-1/2	4	-1	-1/2	+1/2

Table 1. Coefficients in Eqs. (8) and (10).

The coefficient $s_k, r_k,$ and t_k is given in Tab. 1. Similar integral form in Eq. (8) was first introduced in [1] for the purpose of constructing feature detector; however, to best of our knowledge, explicit result of this integral has never appeared in the literature aside from this paper. Compare

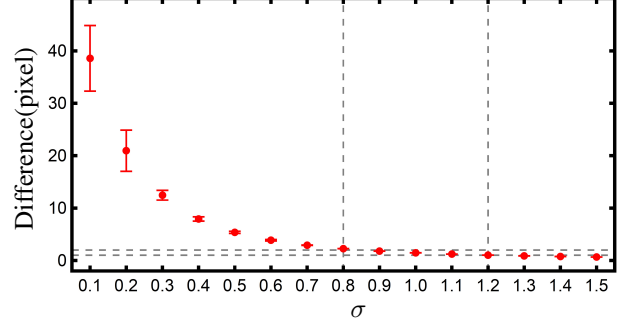


Figure 6. **Maximum difference between Eq. (8) and Eq. (4)**. Samples was taken in a 10×10 pixel region centered at \mathbf{q} . The feature center is randomly selected within a one-pixel range, and the angle is randomly chosen between $[0, \pi/4]$. $W = 200$ and $B = 50$ for typical gray scale. For each σ , we repeated the experiment 500 times. The two horizontal dashed lines indicate one and two gray levels, and vertical dashed lines represent the closest corresponding σ .

with Eq. (4) we can find that both of them has two part, one is the average intensity, another equals intensity difference times some quantity about the distance of point to line. For pixel value, it also contains a factor with respect to θ and σ .

Fig. 6 shows the difference between Eq. (8) and Eq. (4), where letter use the center position of pixel. We randomly select the tilt angle of the line and randomly vary the position of \mathbf{q} within the range of one pixel. It can be observed that, under typical image parameters, the maximum difference between the pixel center intensity and the pixel value becomes negligible when σ approaches one pixel. This condition is easily satisfied during calibration, and is also necessary for our refinement algorithm.

3.3. Cost function in feature refinement

For the formulas provided in the previous section, a direct approach is to perform nonlinear optimization on the pixel values. Considering that the checkerboard corners are the intersection points of two lines, for the effects of aliasing in checkerboard corner's center, though the pattern using a display device proposed by Ha et al. [10] can be used to mitigate it. However, not all cameras' point spread functions can be approximated by a Gaussian function. In the generic camera model, elliptical Gaussians are also used as a defocus model [9], but in this case, it is difficult to obtain a simple analytical expression. Generally, a Gaussian approximation of the point spread function can only be applied in the cases of simple apertures and small defocus[19].

Schöps et al. developed a feature refinement method that can be applied to a multi-intersecting line pattern [25], which is a generation of checkerboard. Their method was

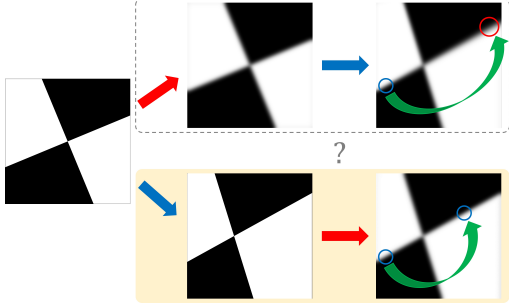


Figure 7. **Two ways of blur nature.** The dashed box above represents a camera that may capture infrared light, while the one below represents a typical optical camera to capture blur image, where defocus is the dominant factor. Blue and red arrows indicate perspective effects and blurring, respectively. The circles correspond to two regions in object space that are symmetric. The former is determined by the homography matrix, and for constant defocus, the latter remains symmetric.

to minimize a symmetrical function

$$\arg \min_{\mathbf{H}} \sum_{i=1}^n (I(\mathbf{H}(s_i)) - I(\mathbf{H}(-s_i)))^2, \quad (11)$$

where s_i is the position in world coordinate centered at every pattern center, and \mathbf{H} is the homography that projects the world coordinate into image pixels. By using the Levenberg-Marquardt(LM) algorithm, they estimates the homography matrix for every feature, the result points was derived from the homography matrix. This method makes significant result better than OpenCV for star-shaped pattern.

However, we believe this method has two limitations: Firstly, Eq. (11) implicitly assumes that the image is captured by a pinhole camera of a continuous physical pattern, this may hold for infrared camera since the surface temperature of an object can hardly change abruptly. But for common used optical cameras, the blur in image is mainly caused by defocus[9, 10, 34]. Secondly, distortion may also leads to a poor initialization of LM algorithm. Moreover, although straight lines can still be considered straight in a small neighborhood despite distortion, which is why the chessboard method is effective. But when number of intersection lines large than two, the mapping of these lines may not be described by a homography under distortion.

Now let's do a more physical modification of Eq. (11). Firstly we assume that the Gaussian kernel is a suitable approximation for point spread function. Within the pixel ranges used for calibration, the Gaussian σ of kernel function can be considered a constant. This assumption works well even with large defocus up to several tens of pixels [11], though in that case we should consider the environment light change. We cannot use a single homography

matrix to describe this mathematical relationship. A homography matrix has eight degrees of freedom and can be determined by the correspondence of four pairs of points. Considering two intersecting lines in a checkerboard pattern, a homography matrix can be computed by selecting a bounding box around any one of the blur lines. However, the pixels near the other blur line are not necessarily determined by this matrix. In fact, the other line can be at any arbitrary angle. But from Eq. (4), we can see that as long as two points are on the same side of the half-plane and equidistant from the boundary line, they have the same value. Furthermore, when another line exists, i.e., in the standard checkerboard pattern, if two points are symmetric with respect to the feature point \mathbf{q} , then they have the same value. Therefore, we can formulate the following optimization objective

$$\arg \min_{\mathbf{q}} \sum_i [\mathcal{I}_{pt}(\mathbf{q} + \Delta_i) - \mathcal{I}_{pt}(\mathbf{q} - \Delta_i)]^2. \quad (12)$$

Similar to [25], we randomly sample sub-pixel points Δ_i and then optimized it by LM algorithm. The Jacobian is calculated by bilinear interpolation of the discrete gradient as well. Notice that Eq. (12) only requires the symmetry of kernel function, we actually do not need to know the analytical expression of \mathcal{I}_{pt} .

An additional situation needs to be discussed: if the window size exceeds the physical size of the pattern(Fig. 8), our cost function may not yield good results, and the method of Schöps et al. would be more suitable. However, considering that we always set the optimization window small enough (around 20 pixels) in calibration for more accurate distortion calculations, and to better utilize the pattern information and avoid aliasing, we believe that in this case, the priority should be to adjust the physical size of the pattern.



Figure 8. **Abnormal condition.** If the size of optimization window (red box) exceeds size of the pattern, our cost function will become unsuitable.

4. Evaluation

4.1. Experiment Setup

Many previous studies have achieved excellent results on synthetic data but performed a little bit poorly on real data;

therefore, we only use real data for evaluation. We evaluate our method on two datasets: one is the star-pattern dataset provided by Schöps et al., and the other consists of results captured using the Intel D435 color camera. Our data is obtained as follows: First, we convert the calibration pattern sequence from Fig. 3 into a PDF file, then use the built-in screen recording software on Windows to record the process of flipping through the PDF file, generating a calibration video. We then play this calibration video in a loop and capture the results using D435. From the captured video stream, we compare the average pixel difference between adjacent frames. If it is smaller than a threshold (set to 1 pixel), we consider the frame to be stable. From each stable frame sequence, we select the middle frame and determine the corresponding channel based on the AprilTag index. We are not concerned with the initialization of feature positions, as the initial positions of all features are determined by the star-shaped pattern. We use the generic camera calibration pipeline published by Schöps et al. on GitHub [25] for generic camera parameter calculation. This pipeline provides BA optimization for various camera models including Brown-Conrady, Thin-Prism Fisheye and generic model.

We primarily evaluate accuracy using the direction of the reprojection error, the median reprojection error (MRE), and the KL-Divergence between scaled distribution of reprojection error and 2D normal distribution, which is used by Schöps et al. for metric of biasedness. Additionally, we compare the computational time difference between our cost function and that of Schöps et al. with no CUDA.

4.2. Evaluation of cost functions

To evaluate our cost function, we used the calibration data provided by Schöps et al. on GitHub (issue 16) [25], which includes 1379 images captured by a D435 infrared camera. Splitting the data into training and test sets is not a common practice for camera calibration evaluation, all data were used. We run the feature extraction and generic camera calibration pipeline provided by Schöps et al., with the parameter setting optimized for a window half-width of 10 pixels, and the cost function computed the image intensity difference.

Method	MRE (pixels)	KL Divergence	Average time (seconds)
Schöps et al.	0.0532	0.50	2.3
Proposed	0.0326	0.49	0.41

Table 2. Evaluation of cost functions.

From Tab. 2, our method reduces the MRE by 38% compared to the method of Schöps et al., and the computation time is reduced to less than 1/5. Fig. 9 shows that both two methods achieve relatively uniform directions of reprojection

error under the central generic model, without introducing strong systematic errors.

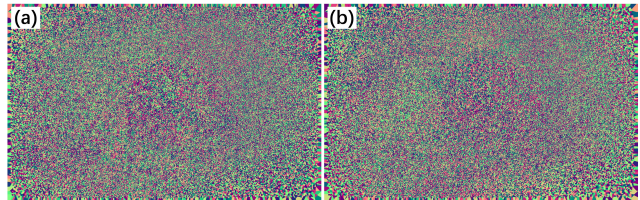


Figure 9. **Reprojection error directions.** (a) Schöps et al.'s method (b) Proposed. Evaluated with 1379 images and central generic camera model.

We do not expect significant differences between our method and that of Schöps et al.'s when the calibration pattern are mostly parallel to the camera plane. However, for datasets like those with many non-parallel images, and in cases where infrared illumination is not used, the D435 primarily captures visible light calibration patterns. In such situations, the advantages of our method can be anticipated.

4.3. Evaluation of calibration patterns

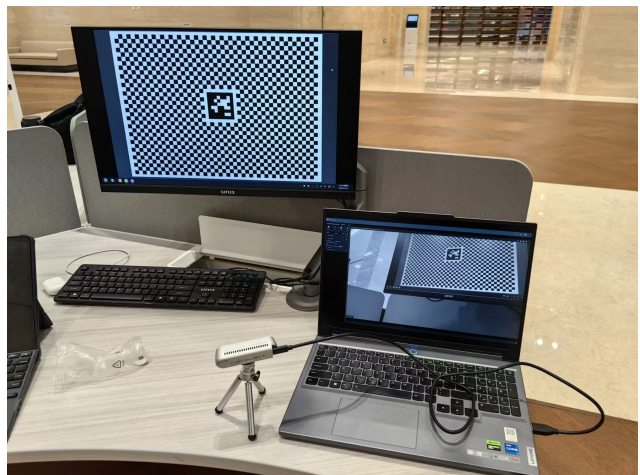


Figure 10. **Experiment setup.** The calibration video is played on a screen and then captured by Intel D435 color camera, which has resolution 1920×1080 and FOV of $70^\circ \times 42^\circ$.

In the current implementation of pattern, the proposed scheme requires more time to capture each target during calibration compared to the static pattern. As a result, it is difficult to obtain thousands of calibration images by simply recording a video, making it challenging to calibrate a general camera model that requires dense data using manual methods. Therefore, we test using a simple Brown-Conrady model. We use 12 parameters, including 4 camera matrix elements, 6 radial distortion parameters, and 2 tangential

distortion parameters. While this calibration method is implemented in OpenCV, considering the refraction correction issue mentioned by Ha et al.[10], we use the implementation of Schöps et al. [25] which including BA correction.

We evaluated three calibration patterns: one is the checkerboard pattern, or 4-segment star pattern; the second is 16-segment pattern proposed by Schöps et al., which showed the best calibration accuracy in their experiments; and the last is proposed pattern. Our pattern uses two different numbers of rotating checkerboard: one with 4, corresponding to the pattern proposed by Schöps et al., with the same black-and-white segments, and the other with 8.

Pattern	Method	MRE (pixels)	KL Divergence
Star-4	Proposed	0.085	2.24
Star-4	OpenCV	0.096	2.18
Star-16		0.071	2.14
Mult-4	Proposed	0.066	2.16
Mult-8		0.055	2.13

Table 3. **Evaluation of calibration patterns.** *Star-n* refers to a star-shaped pattern with n segments, *Star-4* is just the checkerboard pattern plus an AprilTag. *Mult-n* refers to the n sets of rotated checkerboard patterns that we propose.

We summarized the experimental results in the Tab. 3, compared to the star-shaped calibration pattern with the same number of black-and-white segments, our method reduces the MRS by 7.0%. Compared to using the checkerboard pattern and OpenCV feature refinement, our pattern with 8 rotating checkerboard reduces the reprojection error by 42.7%. Our experiment used 27 images, which is sufficient for parameterized camera model calibration. Additionally, we followed the approach of Schöps et al. by using a pattern with more control points than the standard chessboard. While typical experiments involve around 100 points, each of our extracted feature points ranged from 200 to 400. Such results are significant.

5. Discussions

Conclusion In this paper, we introduced a novel approach to camera calibration, focusing on both pattern and cost function design. Our method demonstrated significant improvements over previous techniques in terms of both accuracy and computational efficiency. Specifically, in a dataset with more than one thousand images provide by Schöps et al. for generic camera calibration, our cost function reduced the median reprojection error by 38% compared to their method, while also decreasing computation time by more than 80%. The proposed dynamic calibration pattern, based on rotating checkerboard sequences, further enhanced accuracy, achieving a 42.7% reduction in repro-

jection error compared to traditional checkerboard-based methods with OpenCV feature refinement. Our method provides new insights for high-precision generic camera calibration and structured light design. We also discussed the impact of interpolation on existing symmetry-based cost functions through the analytical expression of the defocus model. We used a Gaussian kernel for the calculation, and give the analytical expression of pixel integral. Under typical parameters, our results show that when the Gaussian sigma is around just 1 pixel, the difference between pixel area integral and the pixel center can be ignored. Therefore, our cost function based on interpolation techniques can be effective in conventional camera calibration.

Limitations and feature works We tested our calibration pattern on the standard Brown-Conrady model, which inevitably introduces systematic errors. To apply it to a generic model, we need to further engineer and optimize the implementation of the proposed pattern to enhance its data acquisition speed. Additionally, we have experimentally validated that multiple checkerboard patterns can achieve higher calibration accuracy compared to the star-shaped pattern. However, we have not yet discussed the limits of pattern amounts. A quantitative idea is illustrated in the Fig. 11 bellow: we need to distinguish the two adjacent segments at the edge of the optimization window, ensuring they fall on different pixels. For a window with half-width of r , at most $2\pi r$ segments can be resolved. However, we need to account for defocus and interpolation effects, which make the precise computation of results difficult, and this requires further research.

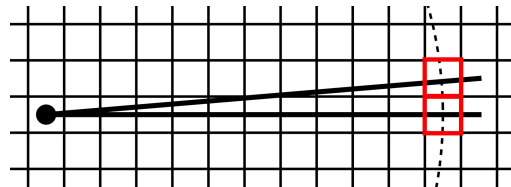


Figure 11. **What is the resolution limit?** Dashed line represents a circular range with a radius equal to the half-width of the feature refinement window.

There is one issue that should be mentioned again, although we used a screen to display our calibration pattern, it does not rely on the display device in the same way as other dynamic markers. In fact, if we change the bounding shape of our pattern from square to circular, we can manufacture it mechanically and drive it with motors. This would make it applicable in situations where a display cannot be used, and this will be the focus of our next experimental direction.

References

- [1] Simon Baker, Shree K Nayar, and Hiroshi Murase. Parametric feature detection. *International Journal of Computer Vision*, 27(1):27–50, 1998. 3, 4, 5
- [2] Bolin Cai, Yuwei Wang, Jiajun Wu, Mengyu Wang, Fei Li, Mengchao Ma, Xiangcheng Chen, and Keyi Wang. An effective method for camera calibration in defocus scene with circular gratings. *Optics and Lasers in Engineering*, 114: 44–49, 2019. 3
- [3] Ankur Datta, Jun-Sik Kim, and Takeo Kanade. Accurate camera calibration using iterative refinement of control points. In *2009 IEEE 12th International Conference on Computer Vision Workshops, ICCV Workshops*, pages 1201–1208. IEEE, 2009. 1, 2, 4
- [4] Frederic Devernay and Olivier Faugeras. Straight lines have to be straight. *Machine vision and applications*, 13:14–24, 2001. 1
- [5] C Brown Duane. Close-range camera calibration. *Photogramm. Eng.*, 37(8):855–866, 1971. 1
- [6] Alexander Duda and Udo Frese. Accurate detection and localization of checkerboard corners for calibration. In *BMVC*, 2018. 2
- [7] John G Fryer and Duane C Brown. Lens distortion for close-range photogrammetry. *Photogrammetric engineering and remote sensing*, 52:51–58, 1986. 1
- [8] Wolfgang Förstner and Eberhard Gülch. A fast operator for detection and precise location of distinct points, corners and centres of circular features. In *Proc. ISPRS intercommission conference on fast processing of photogrammetric data*, pages 281–305. Interlaken, 1987. 2
- [9] Michael D Grossberg and Shree K Nayar. A general imaging model and a method for finding its parameters. In *Proceedings Eighth IEEE International Conference on Computer Vision. ICCV 2001*, pages 108–115. IEEE, 2001. 1, 5, 6
- [10] Hyowon Ha, Yunsu Bok, Kyungdon Joo, Jiyoung Jung, and In So Kweon. Accurate camera calibration robust to defocus using a smartphone. In *Proceedings of the IEEE International conference on computer vision*, pages 828–836, 2015. 3, 4, 5, 6, 8
- [11] Hyowon Ha, Michal Perdoch, Hatem Alismail, In So Kweon, and Yaser Sheikh. Deltile grids for geometric camera calibration. In *Proceedings of the IEEE International Conference on Computer Vision*, pages 5344–5352, 2017. 2, 6
- [12] Janne Heikkilä. Geometric camera calibration using circular control points. *IEEE Transactions on pattern analysis and machine intelligence*, 22(10):1066–1077, 2000. 1
- [13] Janne Heikkilä and Olli Silven. Calibration procedure for short focal length off-the-shelf ccd cameras. In *Proceedings of 13th International Conference on Pattern Recognition*, pages 166–170. IEEE, 1996. 1
- [14] Daniel Herrera, Juho Kannala, and Janne Heikkilä. Joint depth and color camera calibration with distortion correction. *IEEE Transactions on Pattern Analysis and Machine Intelligence*, 34(10):2058–2064, 2012. 1
- [15] Junzhou Huo, Haidong Zhang, Zhichao Meng, Fan Yang, and Guiyu Yang. A flexible calibration method based on small planar target for defocused cameras. *Optics and Lasers in Engineering*, 157, 2022. 3
- [16] Juho Kannala and Sami S Brandt. A generic camera model and calibration method for conventional, wide-angle, and fish-eye lenses. *IEEE transactions on pattern analysis and machine intelligence*, 28(8):1335–1340, 2006. 1
- [17] Kang Liao, Lang Nie, Shujuan Huang, Chunyu Lin, Jing Zhang, Yao Zhao, Moncef Gabbouj, and Dacheng Tao. Deep learning for camera calibration and beyond: A survey. *arXiv preprint arXiv:2303.10559*, 2023. 1
- [18] Luca Lucchese and Sanjit K Mitra. Using saddle points for subpixel feature detection in camera calibration targets. In *Asia-Pacific Conference on Circuits and Systems*, pages 191–195. IEEE, 2002. 2
- [19] Fahim Mannan and Michael S Langer. What is a good model for depth from defocus? In *2016 13th Conference on Computer and Robot Vision (CRV)*, pages 273–280. IEEE, 2016. 5
- [20] Zhichao Meng, Haidong Zhang, Doudou Guo, Shangqi Chen, and Junzhou Huo. Defocused calibration for large field-of-view binocular cameras. *Automation in Construction*, 147:104737, 2023. 3
- [21] Vishvijit S Nalwa and Thomas O Binford. On detecting edges. *IEEE transactions on pattern analysis and machine intelligence*, (6):699–714, 1986. 3, 4
- [22] Zoltan Pusztai and Levente Hajder. Accurate calibration of lidar-camera systems using ordinary boxes. In *Proceedings of the IEEE international conference on computer vision workshops*, pages 394–402, 2017. 1
- [23] Srikumar Ramalingam and Peter Sturm. A unifying model for camera calibration. *IEEE transactions on pattern analysis and machine intelligence*, 39(7):1309–1319, 2016. 1
- [24] Thomas Schops, Torsten Sattler, and Marc Pollefeys. Bad slam: Bundle adjusted direct rgb-d slam. In *Proceedings of the IEEE/CVF Conference on Computer Vision and Pattern Recognition*, pages 134–144, 2019. 2
- [25] Thomas Schops, Viktor Larsson, Marc Pollefeys, and Torsten Sattler. Why having 10,000 parameters in your camera model is better than twelve. In *Proceedings of the IEEE/CVF Conference on Computer Vision and Pattern Recognition*, pages 2535–2544, 2020. 1, 2, 3, 5, 6, 7, 8
- [26] Chaehyeon Song, Jaeho Shin, Myung-Hwan Jeon, Jongwoo Lim, and Ayoung Kim. Unbiased estimator for distorted conics in camera calibration. In *Proceedings of the IEEE/CVF Conference on Computer Vision and Pattern Recognition*, pages 373–381, 2024. 2
- [27] Agustín Trujillo-Pino, Karl Krissian, Miguel Alemán-Flores, and Daniel Santana-Cedrés. Accurate subpixel edge location based on partial area effect. *Image and vision computing*, 31(1):72–90, 2013. 2, 3, 4
- [28] Rafael Grompone von Gioi and Gregory Randall. A sub-pixel edge detector: an implementation of the canny/vernavay algorithm. *Image Processing On Line*, 7: 347–372, 2017. 3
- [29] Shaoan Wang, Mingzhu Zhu, Yaoqing Hu, Dongyue Li, Fulong Yuan, and Junzhi Yu. Accurate detection and localization of curved checkerboard-like marker based on quadratic

- form. *IEEE Transactions on Instrumentation and Measurement*, 71:1–11, 2022. [2](#)
- [30] Yuwei Wang, Lu Liu, Bolin Cai, Keyi Wang, Xiangcheng Chen, Yajun Wang, and Bo Tao. Stereo calibration with absolute phase target. *Optics Express*, 27(16):22254–22267, 2019. [3](#)
- [31] Juyang Weng, Paul Cohen, and Marc Herniou. Camera calibration with distortion models and accuracy evaluation. *IEEE Transactions on Pattern Analysis and Machine Intelligence*, 14(10):965–980, 1992. [1](#)
- [32] Zhengyou Zhang. A flexible new technique for camera calibration. *IEEE Transactions on pattern analysis and machine intelligence*, 22(11):1330–1334, 2000. [1](#)
- [33] Hongbo Zhao, Yikang Zhang, Qijun Chen, and Rui Fan. Dive deeper into rectifying homography for stereo camera online self-calibration. In *2024 IEEE International Conference on Robotics and Automation (ICRA)*, pages 14479–14485. IEEE, 2024. [1](#)
- [34] Shaojie Zhuo and Terence Sim. Defocus map estimation from a single image. *Pattern Recognition*, 44(9):1852–1858, 2011. [3](#), [4](#), [6](#)